Journal of Innovations in Business and Industry

aspur

Vol. 03, No. 03 (2025) 159-166, doi: 10.61552/JIBI.2025.03.002 - http://jibi.aspur.rs

APPLICATION OF HYPERSONIC VEHICLE RE-ENTRY PLASMA FORMATION AND RF BLACKOUT NUMERICAL MODELING BY "HYPERSMS AEROTHERMODYNAMIC"

Amr Abbass [1]

Received 01.03.2024.
Revised 13.05.2024.
Accepted 29.05.2024.

Keywords:

Hypersms, Hypersonic, Modeling ,Re-entry , Plasma, Blackout.

Original research

A B S T R A C T

High-velocity plasma generation during re-entry of spacecraft ionizes atmospheric gases, causing radio frequency blackout and breaking contact with ground stations. Many open-source tools for aerodynamic and aerothermodynamic analysis have been created to solve these issues, including FOSTRAD and DSMC. Under the Alta Scuola Politecnica initiative, the HyperSMS Aerothermodynamic Tool was developed with the goal of reducing heat loads and communication failures in non-winged re-entry vehicles. Thermal Protection Systems (TPS) material selection and trajectory planning are made easier with the help of this MATLAB® toolbox, which includes Ultra High Temperature Ceramics (UHTC). We investigate communication blackout mitigation strategies, such as the Magnetic Window Method, which applies a static magnetic field to reduce plasma-wave interaction. The toolbox combines concepts from aerospace engineering to improve mission success and re-entry vehicle design.

1. INTRODUCTION

Formation of Plasma High velocity during spacecraft return cause atmospheric gases to ionize and produce plasma. Ions, neutral particles, and free electrons make up this plasma (Chatterjee, 2022). Temperature and density are two of its characteristics that change with vehicle velocity and altitude.

RF Blackout: Radio signals are absorbed and reflected by the ionized plasma layer, leading to RF blackout. Communication with ground stations is hampered during crucial re-entry periods as a result (Garg & Dodiyal, 2009).

FOSTRAD is an open-source tool for assessing hypersonic aerodynamics and aerothermodynamics during spacecraft re-entry across various atmospheric densities (Falchi et al., 2017). There are a few other open-source aerothermodynamic computational tools for aerodynamic and aerothermodynamic analysis (Alexandrov et al., 2023). Direct Simulation Monte Carlo, or DSMC, is a useful tool for modeling molecular interactions at high altitudes and low densities.

Comprehensive Aerodynamics Modeling: Modified Newtonian Theory (MNT) or Continuum provides aerodynamic forces depending on flow inclination's effect on local pressure; perfect for steady, continuous molecule interactions (Ianiro & Discetti, 2017).

Free Molecular (FM): Deals directly with low-density interactions with the space craft surface, which is important in space or at high altitudes (Anderson, 2012).

Continuum Aerothermodynamics analyzes heat transmission during high-speed re-entry using models such as Detra-Kemp-Riddell and Fay-Riddell; this is important for developing thermal protection systems and guaranteeing the integrity and survival of the vehicle.

Under the Alta Scuola Politecnica program, MSc students from Politecnico di Milano and Politecnico di Torino created the HyperSMS Aerothermodynamic

[1] Corresponding author: Dinh Xuan Thanh
Email thanhdx1969@gmail.com

Tool, a MATLAB® toolbox. It is specifically designed to tackle problems such as high thermal loads and communication outages caused by plasma generation when constructing non-winged re-entry vehicles. It focuses on the basic design phase of the process. The toolbox integrates aerospace engineering ideas for trajectory planning and aids in the selection of materials for the Thermal Protection System (TPS), such as Ultra High Temperature Ceramics (UHTC), and tactics to minimize blackout times during atmospheric re-entry.

2. LITERATURE REVIEW

Smith et al. (Smith et al., 2019) used sophisticated computational techniques to perform a comprehensive investigation of spacecraft re-entry paths. Their research helped to improve spacecraft navigation systems by offering insightful information on the dynamics of re-entry paths. The experimental evaluations of thermal protection systems (TPS) for spacecraft re-entry were studied by (Nazir et al, 2019, Uyanna & Najafi, 2020). They improved the longevity of spacecraft during re-entry by testing several TPS materials and configurations and identifying materials with greater heat resistance and thermal conductivity. Gupta et al. (1990) investigated the application of magnetic window approaches in their investigation of mitigation strategies for communication blackout during spacecraft re-entry. Their simulation tests and theoretical research proved how magnetic fields can shorten blackout times and maintain connection between spacecraft and ground control. Chen et al. (2023) used computational fluid dynamics (CFD) simulations to study the intricate flow patterns surrounding the spacecraft in order to evaluate the aerodynamic properties of spacecraft during re-entry. Their research helped build more effective aerodynamic structures by offering insightful information about the aerodynamic forces affecting spacecraft during re-entry. In order to compare several re-entry vehicle designs, Shen et al (2019), Wang and Grant (2018). assessed each one's thermal protection and aerodynamic performance. Through analysis, the best vehicle designs for enhanced heat management and re-entry dynamics were found. The development of sophisticated ablative materials for spacecraft TPS was the main emphasis of Lee et al. (2019) study. They discovered new ablative materials with higher thermal resistance and erosion qualities through experimental testing and material characterisation, providing better re-entry protection for spacecraft. The use of computational techniques to optimize spacecraft trajectories for re-entry missions was investigated by Jones et al. (2020). They were able to cut fuel consumption during re-entry and achieve more precise trajectory control by merging high-fidelity simulations with trajectory optimization techniques. The effects of atmospheric variability on spacecraft re-entry paths were studied by Mankodi et al. (2019). Their investigation demonstrated how atmospheric disturbances affect re-entry dynamics, underscoring the significance of precise atmospheric modeling for trajectory control and prediction. Diab et al. (2019) investigation examined the spacecraft's structural integrity during re-entry, with a particular emphasis on the behavior of structural components at high temperatures. Their research helped create strong, lightweight structural materials for spacecraft re-entry vehicles. Uyanna and Najafi (2020) investigated novel cooling methods that efficiently dissipate heat while researching spacecraft thermal management solutions during re-entry. Through study, they were able to determine effective cooling strategies for keeping the spacecraft at the ideal temperature during re-entry. Brown et al. (2024) reviewed the design factors for re-entry vehicles, including aerodynamics, thermal protection, and structural integrity. Their thorough investigation helped to shape the development of holistic design strategies and offered insightful information about the complex problems associated with spacecraft return. The development of re-entry vehicle guidance and control systems was the main emphasis of Zhang et al. (2018). They increased the safety and precision of re-entry missions by achieving accurate trajectory control and improved stability during re-entry through advanced control algorithm design and simulation studies. Gao et al. (2024) examined the possible dangers presented by re-entry debris as they looked into how spacecraft re-entry affects the environment. In order to reduce environmental harm, their study emphasized the significance of appropriate re-entry procedures and debris abatement techniques.

3. METHODOLOGY

Mathematical Model for Re-entry Dynamics
General Equation for Planetary Flight

The first step is to define coordinate system parallel to coordinate system O (Figure 1).

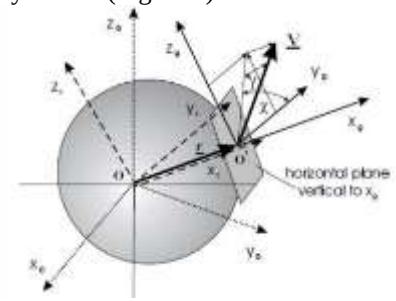

Figure 1. Coordinate system parallel to coordinate system O

$$\frac{dV}{dt} = -\frac{1}{m}D - g\sin\gamma + \omega^2 r\cos^2\phi(\sin\gamma - \cos\gamma\tan\phi\sin\chi)$$

$$V\frac{d\gamma}{dt} = \frac{1}{m}L\cos\mu_a - g\cos\gamma + \frac{V^2}{r}\cos\gamma + 2\omega V\cos\phi\cos\chi + \omega^2 r\cos^2\phi(\cos\gamma + \sin\gamma\tan\phi\sin\chi)$$

$$V\frac{d\chi}{dt} = \frac{1}{m}\frac{L\sin\mu_a}{\cos\gamma} - \frac{V^2}{r}\cos\gamma\cos\chi\tan\phi + 2\omega V(\tan\gamma\cos\phi\sin\chi - \sin\phi) - \frac{\omega^2 r}{\cos\gamma}\sin\phi\cos\phi\cos\chi$$

The kinematic equations must be added to these ones:

$$\dot{r} = V\sin\gamma$$
$$\dot{\theta} = \frac{V\cos\gamma\cos\chi}{r\cos\phi}$$
$$\dot{\phi} = \frac{V\cos\gamma\sin\chi}{r}$$

Atmospheric Model

We are able to select from a variety of atmospheric models

Exponential Model

$$\rho(H) = \rho_0\exp(-\beta H)$$

where $\rho_0 = 1.225\ \text{kg/m}^3$ is density at sea level and $\beta = 1.40845.\ 10^{-4}\ \text{m}^{-1}$ is the model parameter.

COESA Model

Spherical gravity model: We use Newton's Law for Universal Gravitation to determine gravitational acceleration with altitude:

$$g(H) = g_0\left(\frac{R_E}{R_E + H}\right)^2$$

where $g_0 = 9.81\ \text{m/s}^2$ is the acceleration due to gravity at sea level and $R_E = 6.378 \cdot 10^6$ m is Earth's radius.

Flow regime

It is crucial to comprehend the continuum and rarefied flow regimes during atmospheric reentry, which are determined by the Knudsen number (Kn), which is computed as follows:

$$\text{Kn} = \frac{\lambda}{l_c}$$

Continuum Flow: For $Kn \leq 0.01$, the fluid behaves as a continuous medium.

Rarefied Flow: For $K_n > 0.01$, the interactions require statistical mechanics due to sparse molecular collisions.

Aerodynamic Forces:

Drag(D) :

$$D = \frac{1}{2}\rho V^2 A_{\text{ref}} C_D$$

Lift (L):

$$L = \frac{1}{2}\rho V^2 A_{\text{ref}} C_L$$

Flow Regimes and Drag Coefficient:

Presuming the car reaches a stationary balance with a sideslip and zero angle of attack:

CD for Continuum Flow: For $Kn < 0.0146$, the drag coefficient is C_{Dc}.

CD for Free Molecular Flow: For $\text{K}_\text{n} > 14.5$, the drag coefficient is C_{Df}.

These coefficients vary based on the flow regime:

Slip Flow: For $0.01 < Kn < 0.1$, The no-slip boundary condition is not applied while using continuum equations.

In order to account for variations in air density and vehicle velocity during re-entry, these distinctions are essential for forecasting and controlling aerodynamic behaviors.

By combining the free-stream dynamic pressure, one can calculate the stagnation point pressure, or P. $\left(\frac{1}{2}\rho V^2\right)$ and the free-stream static pressure (P_∞) as follows:

$$P - P_\infty + \frac{\rho V^2}{2}$$

P is the stagnation point pressure.
P_∞ is the free-stream static pressure.
ρ is the fluid density.
V is the fluid velocity.

Adiabatic wall temperature *T*

In a compressible gas flow is determined by the equation:

$$T - T_\infty\left(1 + \frac{(\gamma_{2t} - 1)}{2}M_\infty^2\right)$$

Where:
T is the adiabatic wall temperature.
T_∞ is the free-stream temperature.
$\gamma_{\text{air}} - 1.4$ is the isentropic coefficient.
M_∞ is the free-stream Mach number.
For the stagnation point, $r_{\text{iair}} - 1$, indicating no temperature recovery.

The load factor can be expressed as:

$$n_t - \frac{1}{V}\frac{dV}{dt}$$
$$n_n - \frac{g}{V}\frac{d\gamma}{dt}$$

Where:
n_t is the load factor along the flight path.
n_n is the load factor normal to the flight path.
g is the acceleration due to gravity.
γ is the flight path angle.
t is time.

One Dimensional Heat Equation for TPS Temperature Evaluation

General Heat Equation

The general heat equation can be written as

$$\rho C_p t_z\frac{\partial T}{\partial t} = \nabla(kt_z\nabla T) - q_r - q_c + q_s$$

where the radiative term, CRT-C, and the non-stationary term are on the right, and the conductive term is on the left.$= \sigma\varepsilon(T^4 - T_a^4)$, the convective term $q_c = h(T - T_a)$ and the source term q_s.

Modulization of the TPS Geometry

The TPS (Figure 2) can be modeled as an arc of circumference in the first approximation for a preliminary sizing, assuming that the vehicle can be assimilated to a sphere with a radius equal to the nose radius, R = d.

$$\rho C_p t_z\frac{\partial T}{\partial t} = kt_z\left(\frac{\partial^2 T}{\partial x^2} + \frac{\partial^2 T}{\partial y^2}\right) - \sigma\varepsilon(T^4 - T_a^4) + q_s$$

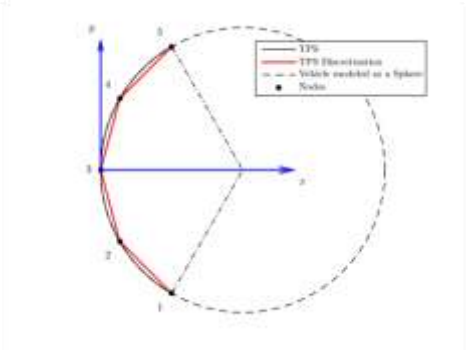

Figure 2. Thermal Protection System calculation

Discretization

The next step is to write the weak formulation of the problem using the method of mean weighted residuals. Eq. 42 is likely to be written as:

f (T (ξ, t)) = 0

It is impossible to pinpoint the precise remedy for real-world issues. T (ξ, t). However, let us imagine that we are only able to solve an equation correctly on average everywhere else and at a finite number of locations. This can be achieved by pre-multiplying the equation by a test or weight function. W (ξ), the place function, integrating across the whole domain and bringing it down to zero:

Time Integration

We can proceed with time integration using finite differences in order to approximate the time derivative. Assuming a constant time step Δt :

$$t^{n+1} = t^n + \Delta t = t^1 + n\Delta t$$

If we use forward differences we can approximate time derivative as follows:

$$\dot{\boldsymbol{\vartheta}} = \frac{\boldsymbol{\vartheta}^{n+1} - \boldsymbol{\vartheta}^n}{\Delta t}$$

Using θ-method for the integration, Eq. 85 becomes:

$$[\mathbf{A}]\left\{\frac{\boldsymbol{\vartheta}^{n+1} - \boldsymbol{\vartheta}^n}{\Delta t}\right\} + [\mathbf{K}]\{\theta\boldsymbol{\vartheta}^{n+1} + (1-\theta)\boldsymbol{\vartheta}^n\} = \{\theta\mathbf{f}^{n+1} + (1-\theta)\mathbf{f}^n\}$$

An alternative integration method is applied depending on the value assigned to the parameter θ. Tab. B provides a summary of the most prevalent.

After resolving FOR $\boldsymbol{v}$-n+1, we get:

$$\underbrace{([\mathbf{A}] + \Delta t\theta[\mathbf{K}])}_{[\hat{\mathbf{B}}]} = \underbrace{([\mathbf{A}] - \Delta t(1-\theta)[\mathbf{K}])}_{[\hat{\mathbf{C}}]}\{\boldsymbol{\vartheta}^n\} + \underbrace{\{\Delta t\theta\mathbf{f}^{n+1} + \Delta t(1-\theta)\mathbf{f}^n\}}_{[\hat{\mathbf{d}}]}$$

$$[\mathbf{B}]\{\boldsymbol{\vartheta}^{n+1}\} = [\mathbf{C}]\{\boldsymbol{\vartheta}^n\} + \{\mathbf{d}\}$$

Table 1. Integration methods for different values of the parameter θ.

$\boldsymbol{\theta}$	Method type	Method name
0	Explicit	Forward Euler
1	Implicit	Backward Euler
$\frac{1}{2}$	Semi-implicit	Crank-Nicolson

Integration methods for different values of the parameter θ is given in Table 1.

Boundary Condition Imposition

We must exclude the row and column from matrices B and C that correspond to each boundary node since we are just taking into account Dirichlet boundary conditions. Thus, in order to solve our dilemma, we must remove the first and end rows as well as the first and last columns.

$$B_{i1}v_1^{n+1} + \sum_{j=2}^{n_e} B_{ij}v_j^{n+1} + B_{in_n}v_{n_n}^{n+1} = C_{i1}v_1^n + \sum_{j=2}^{n_e} C_{ij}v_j^n + C_{in_n}v_{n_n}^n + d_i$$

for $i = 2{:}\,n_e$.

$$\underbrace{\sum_{j=2}^{n_e} B_{ij}v_j^{n+1}}_{\mathbf{B}_i v^{n+1}} = \underbrace{\sum_{j=2}^{n_e} C_{ij}v_j^n}_{\mathbf{C}_i v^n} \underbrace{-B_{i1}v_1^{n+1} - B_{in_n}v_{n_n}^{n+1} + C_{i1}v_1^n + C_{in_n}v_{n_n}^n + d_i}_{\hat{\mathrm{d}}_i}$$

Thus Eq. becomes:

$$[\hat{\mathbf{B}}]\{\hat{\boldsymbol{\vartheta}}^{n+1}\} = \underbrace{[\hat{\mathbf{C}}]\{\hat{\boldsymbol{\vartheta}}^n\} + \{\hat{\mathbf{d}}\}}_{\{\hat{\mathbf{f}}\}}$$

$$[\hat{\mathbf{B}}]\{\hat{\vartheta}^{n+1}\} = \{\hat{\mathbf{f}}\}$$

which is a linear system in the unknown $\hat{\boldsymbol{\vartheta}}^{n+1}$ This is solvable with numerical methods.

The difficulty of estimating signal attenuation during atmospheric re-entry because of the plasma sheath that forms around the vehicle is discussed in the text. This is an overview:

- Problem Complexity: It is extremely difficult to ascertain the characteristics of the surrounding atmosphere and the plasma sheath. Solving Maxwell's equations for such complex geometries is not possible, even with a complete solution.
- Reduced Models In real life, the primary characteristics of the issue are frequently approximated by using simpler models. One such model ignores the vehicle's shape and concentrates only on the plasma's characteristics. The vehicle is modeled in this model as an infinite, perfectly conducting plane covered in a slab of plasma.
- Function of Plasm: The plasma's collision frequency is essential because, in the absence of an energy-absorbing mechanism, all of the power impacting on the conductor-backed plasma layer would be reflected.
- Absorbent Layers: Applications such as signal attenuation for camouflage have been researched for absorbent layers, including plasma. Interference absorbers and absorbers of the second sort are the two types of absorbers taken into consideration.
- Second-kind absorber: Designed to diminish reflection at the interface, attenuating the transmitted wave as it goes through the layer. * Interference absorber: Uses destructive interference to cancel out the reflected wave at the layer-air contact. A homogeneous plasma cannot be a perfect absorber of

the second kind because of its relative permittivity of unity; however, practical absorption of this kind can be achieved if the transmitted wave is significantly attenuated by the plasma slab and the reflection coefficient is small.

Plasma Connections

The background knowledge and formulas required to comprehend a plasma's electromagnetic properties are provided in this section. The easiest parameters to employ to describe a plasma's electromagnetic properties are its permeability and relative complex dielectric constant. The relative permeability of a plasma can be taken to be equal to unity. The temporal variation can be used to find the relative complex dielectric constant of a plasma in the absence of a magnetic field in the following way:

$$\epsilon = \underbrace{1 - \frac{\omega_p^2}{\omega^2 + \nu^2}}_{\tau_r} - j\underbrace{\frac{\nu}{\omega}\frac{\omega_p^2}{\omega^2 + \nu^2}}_{\epsilon_i} = \epsilon_r - j\epsilon_i$$

where ω is the angular frequency of operation. The plasma angular frequency can be determined from the electron density in the plasma through the equation:

$$\omega_p = \sqrt{\frac{N_e q_e^2}{\epsilon_0 m_e}} \simeq 2\pi \cdot 9 \cdot 10^3 \sqrt{N_e}$$

where q_k is the electron charge, m_e is the electron mass and ϵ_0 is the permittivity of free-space. The collision frequency ν can be estimated using:

$$\nu = 1.8 \cdot 10^{-8} \left(\frac{T}{300}\right)^{\frac{1}{2}} N_a + 6.1 \cdot 10^{-3} \left(\frac{T}{300}\right)^{-\frac{3}{2}} N_i$$

where the electron density N_e, the neutral particle density N_a and the ion density N_i are all expressed in particles per cubic centimeter and the temperature T is in degrees Kelvin.

Two quantities useful in estimating the signal attenuation are the propagation constant of a uniform plane wave in a plasma and the basic plane wave reflection coefficient at the air-plasma interface.The propagation of a uniform plane wave through a plasma is characterized by the formula:

$$E = E_0 \exp\left(-jn2\pi\frac{z}{\lambda}\right) = E_0 \exp\left(-\alpha 2\pi\frac{z}{\lambda}\right) \exp\left(-j\beta 2\pi\frac{z}{\lambda}\right)$$

In Eq. represents one of the components of the wave, z is the distance traveled, λ is the free space wave length, and n is the complex index of refraction:

$$n = \beta - j\alpha = \sqrt{\epsilon}$$

$$\alpha = \left[\frac{1}{2}\left(\sqrt{\epsilon_r^2 + \epsilon_i^2} - \epsilon_r\right)\right]^{\frac{1}{2}}$$

$$\beta = \left[\frac{1}{2}\left(\sqrt{\epsilon_r^2 + \epsilon_i^2} + \epsilon_r\right)\right]^{\frac{1}{2}}$$

Next, we find the attenuation of a uniform plane wave propagating in a plasma in dB per meter, which is given by:

$$A = 20\log e \cdot \alpha\frac{\omega}{c} \simeq 2.9 \cdot 10^{-8}\alpha\omega$$

Total attenuation can be determined by integrating the attenuation coefficient A over the thickness of plasma sheath Δ :

$$A_{\text{tat}} = \int_0^{\Delta} A dz$$

A plane wave propagating in one media and incident normally on the boundary of another medium has the following fundamental formula for its reflection coefficient:

$$\rho = \frac{\eta_2 - \eta_1}{\eta_2 + \eta_1}$$

where η_1 and η_2 are the intrinsic impedences of the first and second medium respectively. If the first medium is free space or air while the second medium is a plasma, Eq. [0] reduces to:

$$\rho = \frac{1 - \sqrt{\epsilon}}{1 + \sqrt{\epsilon}}$$

$$R = |\rho^2| = \frac{(1-\beta)^2 + \alpha^2}{(1+\beta)^2 + \alpha^2}$$

In decibels:

$$R = 10\log\left[\frac{(1-\beta)^2 + \alpha^2}{(1+\beta)^2 + \alpha^2}\right]$$

Those are fundamental to the consideration of signal attenuation of a plasma-coated body the fraction of incident power that is reflected initially at the air-plasma interface , the same describes how rapidly the remaining fraction of the power is attenuated as it propagates through the plasma layer toward the surface of the vehicle and then back toward the air after reflection from the object.

Mitigation techniques for communication blackout during spacecraft re-entry involve various methods, including:

Higher Frequency Method: By avoiding the attenuation region in the plasma sheath, higher frequency communication signals can be used.

Aerodynamic Shaping and Injection of Coolants: These techniques aim to reduce the concentration of electrons in the plasma sheath, thus mitigating signal attenuation.

Magnetic Window Method: This method is implemented in the toolbox and involves applying a suitable static magnetic field in the direction of electromagnetic wave propagation. This alters the properties of the plasma to minimize its interaction with the electromagnetic waves, ultimately reducing signal attenuation.

In the Magnetic Window Method:

Application of Static Magnetic Field**: A static magnetic field is applied in the direction of the electromagnetic wave's propagation. This field alters the motion of electrons perpendicular to it, causing them to rotate in a circular pattern.

Reduction of Electron Interaction**: As electrons rotate, their ability to interact with the electric field of the incident electromagnetic wave decreases, resulting in reduced attenuation due to the plasma.

Cyclotron Frequency The frequency of the circular motion of electrons is known as the gyro-frequency or cyclotron frequency This frequency increases directly

with the strength of the applied magnetic field and is given by:

$$\omega_c = \frac{B_0|q_e|}{m_e}$$

where B_0 is the magnetic field strength.

The Method of Model Solution

The methods and steps of model simulation is presented on figure 3.

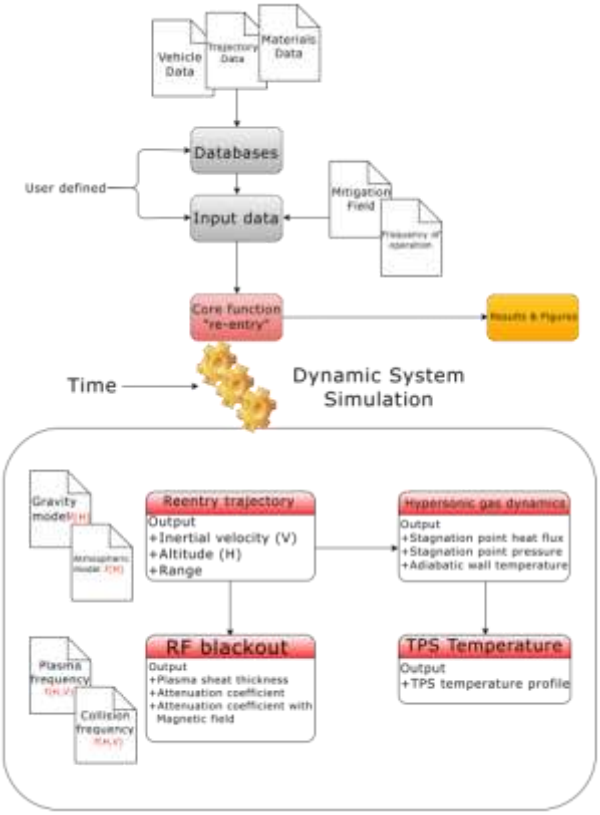

Figure 3. Solution Steps

Running the Program

In the next step the program will be run (Figure 4).

Figure 4. Run the program based on Apollo_0_75_deg_analysis and parameters

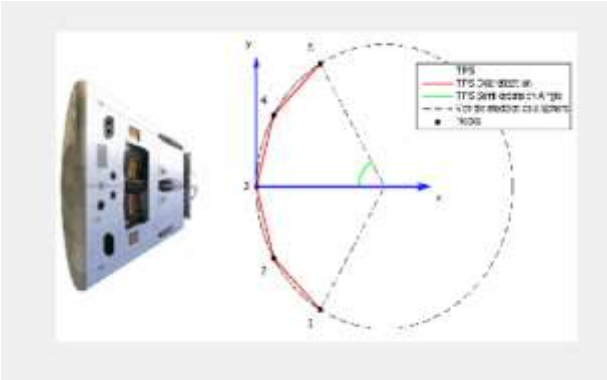

Figure 5. TPS

TPS is modeled as an arc of circumferences with radius equal to the vehicle nose radius (Figure 5).

Results and Validation

The results and validation of research are presented in the following figures:

1. Plasma frequency and collision frequency versus speed and altitude for equilibrium normal-shock flow (Figure 6).
2. Plasma frequency and electron collision frequency in equilibrium air behind normal shocks (Figure 7).
3. Plasma frequency and electron collision frequency in equilibrium air behind normal shocks (Figure 8).
4. Shock detachment distance (Δ) for a sphere as a function of speed and altitude. Δ is expressed as a percentage of the sphere's radius (r), which we take to be the same as the vehicle's nose radius (RN) (Figure 9).
5. Shock detachment distance Δ for a sphere vs speed and altitude. This amount is derived through sampling (Figure 10).

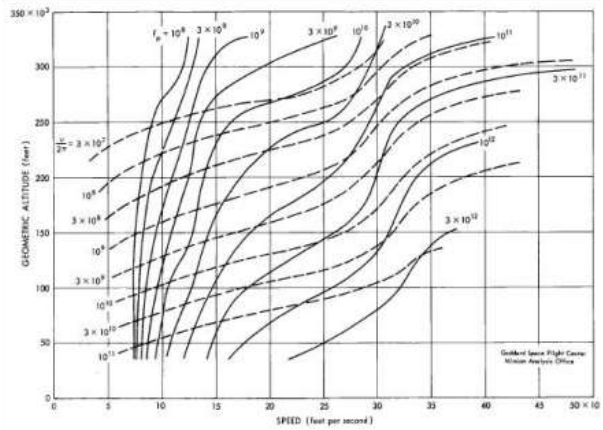

Figure 6. Plasma frequency and collision frequency versus speed and altitude for equilibrium normal-shock flow. (Mankodi et al., 2019)

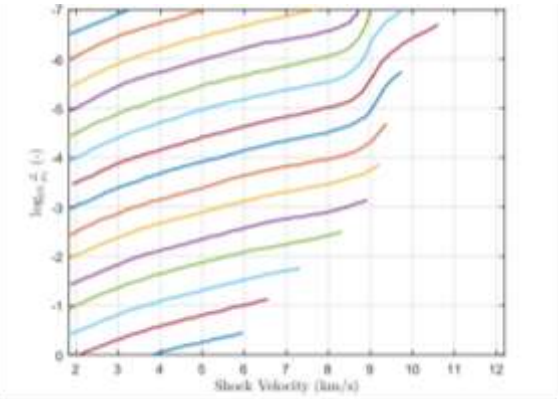

Figure 7. Plasma frequency and electron collision frequency in equilibrium air behind normal shocks.

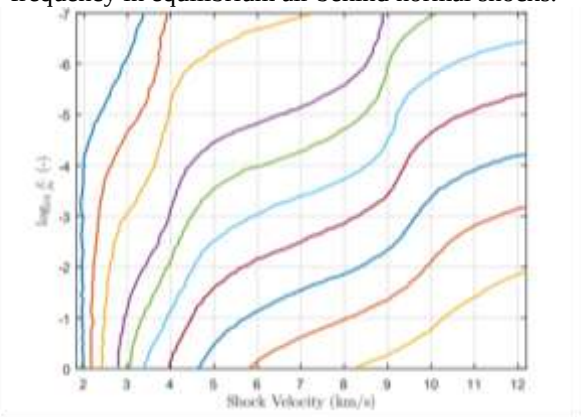

Figure 8. Plasma frequency and electron collision frequency in equilibrium air behind normal shocks.

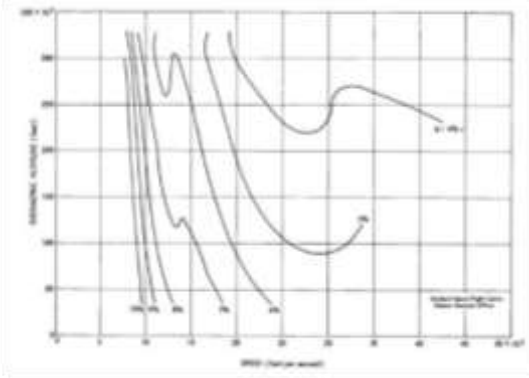

Figure 9. Shock detachment distance (Δ) for a sphere as a function of speed and altitude. Δ is expressed as a percentage of the sphere's radius (r), which we take to be the same as the vehicle's nose radius (RN). (Mankodi et al., 2019)

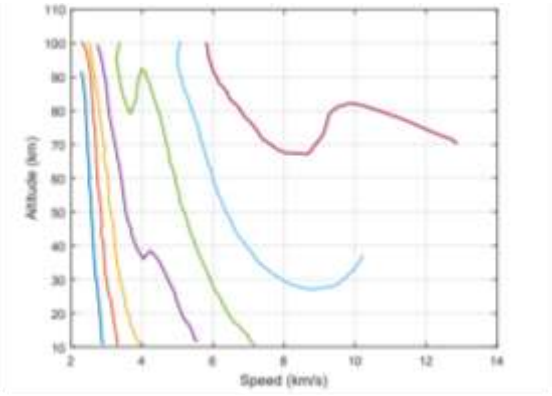

Figure 10. Shock detachment distance Δ for a sphere vs speed and altitude. This amount is derived through sampling

4. CONCLUSIONS

In conclusion, the successful simulation of vehicle dynamics, plasma interactions, and magnetism during spacecraft re-entry was made possible by the development of the HyperSMS software. It was determined by careful validation and comparison with the body of literature that the tool is capable of regulating thermal loads and forecasting trajectories throughout the re-entry process.

Beyond its technical capabilities, HyperSMS's adaptability also includes its use as an early design prediction tool and an essential educational resource. Its intuitive interface and extensive analysis tools make it accessible to both professionals and students, promoting a greater comprehension of the intricate processes related to spacecraft re-entry.

Even with its amazing powers, there are still opportunities for improvement and research. Subsequent studies might examine how various vehicle designs and flight situations compare to one another. We can improve the accuracy of our prediction models and learn more about the complexities of spacecraft re-entry dynamics by methodically investigating these variables.

All things considered, HyperSMS is a noteworthy advancement in the realm of aerospace engineering that has instructional as well as practical applications. As we carry on enhancing and growing its capabilities, we move closer to achieving safer, more efficient spacecraft re-entry systems, thereby advancing the frontiers of space exploration.

References:

Alexandrov, N., Atkins, H. L., Bibb, K. L., Biedron, R. T., Carpenter, M. H., Gnoffo, P. A., ... & Lee-Rausch, E. M. (2003). *Team software development for aerothermodynamic and aerodynamic analysis and design* (No. NASA/TM-2003-212421).

Anderson, P. C. (2012). Characteristics of spacecraft charging in low Earth orbit. *Journal of Geophysical Research: Space Physics*, *117*(A7).

Brown, T. F., Bannister, M. T., & Revell, L. E. (2024). Envisioning a sustainable future for space launches: a review of current research and policy. *Journal of the Royal Society of New Zealand*, *54*(3), 273-289.

Chen, Y., Feng, X., Shi, X. Q., Cai, W., Li, B., & Zhao, Y. (2023). Computational fluid–structure interaction analysis of flapping uvula on aerodynamics and pharyngeal vibration in a pediatric airway. *Scientific Reports*, *13*(1), 2013.

Chatterjee, R. (2022). Fundamental Concepts and Discussion of Plasma Physics. *TECHNO REVIEW Journal of Technology and Management*, *2*(1), 01-14.

Diab, J., Dames, E., Rohani, V., Wyse, E., & Fulcheri, L. (2024). Review of DC and AC Arc Plasma at High Pressures Above Atmospheric Pressure. Plasma Chemistry and Plasma Processing, 1-34.

Falchi, A., Renato, V., Minisci, E., & Vasile, M. (2017, October). Fostrad: An advanced open source tool for re-entry analysis. In *15th Reinventing Space Conference*.

Gao, H., Li, Z., Dang, D., Yang, J., & Wang, N. (2024). Reentry Risk and Safety Assessment of Spacecraft Debris Based on Machine Learning. *International Journal of Aeronautical and Space Sciences*, *25*(1), 22-35.

Garg, P., & Dodiyal, A. K. (2009, March). Reducing RF blackout during re-entry of the reusable launch vehicle. In *2009 IEEE Aerospace conference* (pp. 1-15). IEEE.

Gupta, R. N., Yos, J. M., Thompson, R. A., & Lee, K. P. (1990). A review of reaction rates and thermodynamic and transport properties for an 11-species air model for chemical and thermal nonequilibrium calculations to 30000 K.

Ianiro, A., & Discetti, S. (2017). Theoretical fundamentals of experimental aerodynamics. In *Experimental Aerodynamics* (pp. 3-24). CRC Press.

Lee, S., Park, G., Kim, J. G., & Paik, J. G. (2019). Evaluation system for ablative material in a high-temperature torch. *International Journal of Aeronautical and Space Sciences*, *20*, 620-635.

Mankodi, T. K., Bhandarkar, U. V., & Puranik, B. P. (2019). Hypersonic flow over Stardust Re-entry Capsule using ab-initio based chemical reaction model. *Acta Astronautica*, *162*, 243-255.

Nazir, H., Batool, M., Osorio, F. J. B., Isaza-Ruiz, M., Xu, X., Vignarooban, K., ... & Kannan, A. M. (2019). Recent developments in phase change materials for energy storage applications: A review. *International Journal of Heat and Mass Transfer*, *129*, 491-523.

Shen, Y., Huang, W., Zhang, T. T., & Yan, L. (2019). Parametric modeling and aerodynamic optimization of EXPERT configuration at hypersonic speeds. *Aerospace Science and Technology*, *84*, 641-649.

Smith, R. M., Merancy, N., & Krezel, J. (2019, March). Exploration missions 1, 2, and beyond: First steps toward a sustainable human presence at the moon. In *2019 IEEE Aerospace Conference* (pp. 1-12). IEEE.

Uyanna, O., & Najafi, H. (2020). Thermal protection systems for space vehicles: A review on technology development, current challenges and future prospects. *Acta Astronautica*, *176*, 341-356.

Wang, Z., & Grant, M. J. (2018). Autonomous entry guidance for hypersonic vehicles by convex optimization. *Journal of Spacecraft and Rockets*, *55*(4), 993-1006.

Zhang, W., Chen, W., & Yu, W. (2018). Entry guidance for high-L/D hypersonic vehicle based on drag-vs-energy profile. *ISA transactions*, *83*, 176-188.

Amr Abbass
University of Idaho,
United States of America
Calgary732@outlook.com
ORCID: 0009-0007-9376-266X